

Article

Aerodynamic Drag Reduction by the Trapezoid Spanwise Groove Inspired by Pigeon Feathers

Yanqing Wang, Yuju Wei, Ding Weng * and Jiadao Wang *

State Key Laboratory of Tribology in Advanced Equipment, Tsinghua University, Beijing 100084, China

* Correspondence: dingweng@mail.tsinghua.edu.cn (D.W.); jdwang@mail.tsinghua.edu.cn (J.W.)

Abstract: Inspired by pigeon feathers, the drag-reducing contribution of spanwise grooves was studied. Surface topography of the wing feather was scanned by an instrument of white light interference. Three types of grooves of triangle, rectangle, and trapezoid were adopted based on the unsymmetric microstructures found on the feather surface. Numerical simulations were conducted to analyze drag-reducing mechanisms. According to the simulation results, the rectangular groove reduced the wall shear stress more efficiently but with greater additional pressure drag, while the triangular groove was the opposite. For the trapezoidal groove similar to the feather structure, drag reduction was the best out of the three. Wind tunnel experiments for the trapezoidal groove were performed by using a cylindrical model and large-area plate. Drag reduction was confirmed from the cylindrical model at a series of velocities from 15 m/s to 90 m/s (about 16% at velocity of 30 m/s and about 8.5% at velocity of 60 m/s). Drag reduction was also obtained from the plate model at a velocity range of 30 m/s to 75 m/s (about 19% at the velocity of 60 m/s), which worked for a wide range of velocity and was more meaningful for the application.

Keywords: drag reduction; spanwise groove; bionics



Citation: Wang, Y.; Wei, Y.; Weng, D.; Wang, J. Aerodynamic Drag Reduction by the Trapezoid Spanwise Groove Inspired by Pigeon Feathers. *Energies* **2023**, *16*, 2379. <https://doi.org/10.3390/en16052379>

Academic Editor: Satoru Okamoto

Received: 22 January 2023

Revised: 19 February 2023

Accepted: 22 February 2023

Published: 1 March 2023



Copyright: © 2023 by the authors. Licensee MDPI, Basel, Switzerland. This article is an open access article distributed under the terms and conditions of the Creative Commons Attribution (CC BY) license (<https://creativecommons.org/licenses/by/4.0/>).

1. Introduction

Aerodynamic drag is one of the main problems faced by aircraft and many drag-reducing methods have been studied by researchers. Biological surfaces have unique structures to let them adapt from the natural environment that can be learnt from [1,2]. Inspired by shark skin, it was clearly demonstrated that the riblet surface could reduce the wall shear stress by changing the turbulence boundary layer [3,4]. The drag reduction by different riblet shapes such as sawtooth, semi-circular, and rectangular were studied in experiments [5,6]. The results revealed that the riblet of the sawtooth structure reduced the drag more efficiently than others. The convergent and divergent riblet was also studied, and the velocity distribution near the riblet surface was obtained by experiments [7]. The application research of grooved surfaces was performed, especially in airfoil [8,9]. Numerical simulation provides another way to understand the mechanism of drag reduction. The real shark skin replica was studied by direct numerical simulation, and the results of the simulations were verified by experiments [10]. The numerical studies about different shapes of grooves were also performed and the more flow field details obtained [11,12].

The spanwise groove is another passive drag-reducing method. Although the role of transverse grooves in the drag reduction by bluff bodies has been studied clearly [13–15], their influence on the wall shear stress of flat plates is still unclear. The rectangular spanwise groove was studied by simulation and experiment [16–18]. The result showed that the groove could change the turbulence intensity in the boundary layer. The experiment presents the same results with different spanwise grooves [19]. The drag reduction effect on wall shear stress is related to the shape and size of the groove [20,21], which influences the vortex in the boundary layer [22]. The wall shear stress is important to the drag reduction effect of spanwise grooves, and there are relatively few studies on this aspect.

In previous studies, researchers mostly focused on macro-scale groove structure and the separation control of the boundary layers. However, the micro-scale groove structure mainly acts on the sub-layer of boundary layer of the fluid field, where the viscosity plays a leading role. Inspired by the microstructure of pigeon feathers, we focus on the drag reduction by spanwise micro-grooves. Herein, we performed research on different spanwise grooves using numerical simulation and wind tunnel experiments. The stress and pressure distributions near the groove surface are reported in this paper. The results can help us to understand the drag-reduction mechanism of spanwise grooves clearly.

2. Materials and Methods

2.1. Microstructure of Pigeon Feathers

In the long evolutionary process, birds have evolved their own unique way to reduce aerodynamic drag and pigeons are a typical representative. The structures of pigeon feathers were observed using a three-dimensional white light interference surface topography instrument that can be used for the measurement of surface roughness, three-dimensional surface shape, and microstructure. We collected the feathers that fell off naturally from the wings for morphology observation and no pigeon was injured in this study.

We obtained the three-dimensional surface topography of the wing feathers of pigeons and focused on the groove structure perpendicular to the airflow direction on them. The three-dimensional topography of the wing feather is shown in Figure 1, which presents the topography close to the tip (a) and root (b) of the wing feather. The geometry of the groove structures at different positions are similar to each other. It can be found from the section profile shown in Figure 1 that there are unsymmetric structures between the left and right side of the groove, one side of which is an almost vertical wall, and the other is a sloped wall. This asymmetry was not noticed in previous research. The groove size is different at different positions of the feather, and it is related to the flight speed of pigeons. Combined with the direction of the airflow, we simplified the shape of the groove to a certain extent for later analysis and research, as shown by the dotted line in the section profile in Figure 1.

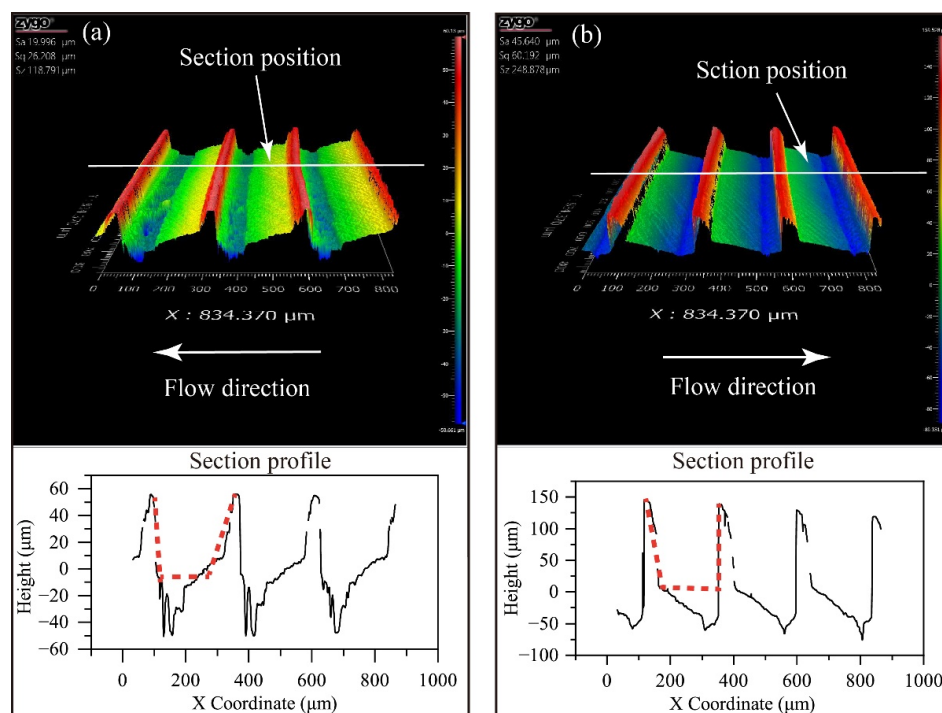


Figure 1. Microscopic morphology of pigeon feathers: (a) the topography and section profile of feather head; (b) the topography and section profile of feather root; the black lines on the section profile are the real shape of feathers and the red dotted lines are the simplified shape of the structures.

2.2. Numerical Approach

2.2.1. Spanwise Groove Geometry and Boundary Conditions

Numerical analysis is a great help to understand the characteristics of the flow field on the surface with spanwise grooves. Here, the two-dimensional simulations were performed based on the geometric features of grooved surfaces. According to the geometry of simplified grooves based on the feather, three typical shapes of triangle, rectangle, and trapezoid were selected in this paper, as shown in Figure 2a. The grooves with two symmetrical structures of triangle and rectangle were designed to analyze the effect of vertical walls and inclined walls. All the grooves were defined by three parameters of width w , depth h , and period p , and the values of that are shown in Table 1. We scaled the size of the grooves because of the low flight speed of the pigeon.

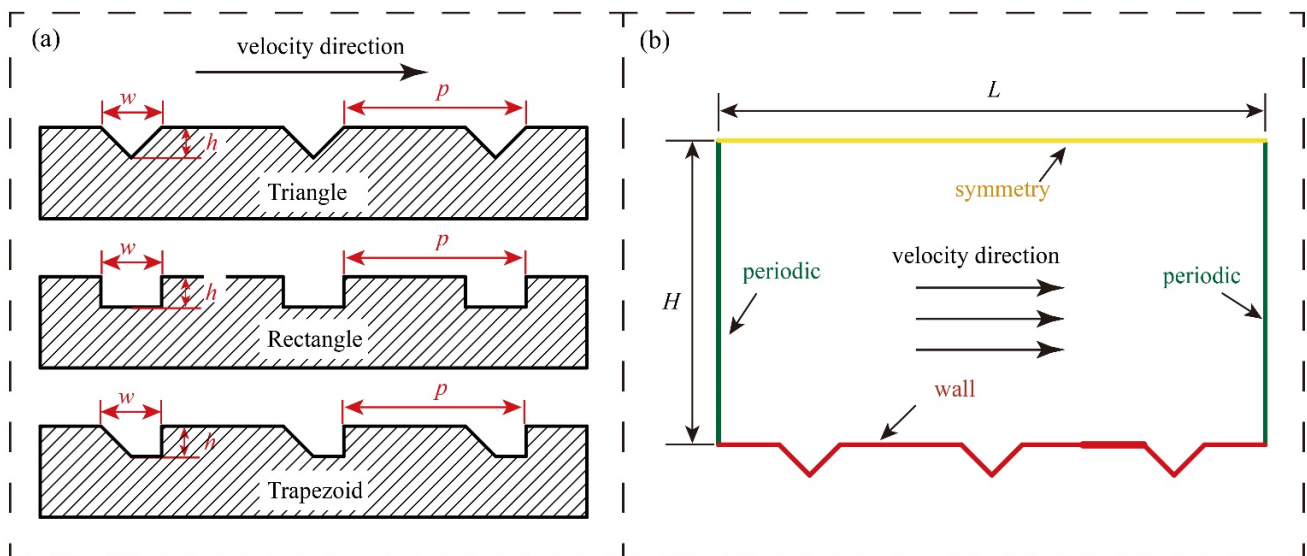


Figure 2. The geometric sketch of the spanwise groove and the computational domain of the CFD simulations: (a) the geometry parameters of three types of grooves; (b) the dimensions of computational domain and the boundary conditions.

Table 1. The parameter values of spanwise groove in the simulations. (Unit: μm).

Groove Type	Parameters	w	p	h
Triangle		40	120	20
Rectangle		40	120	20
Trapezoid		40	120	20

The dimensions of the computational domain are $L = 360 \mu\text{m}$ (three periods) in the streamwise direction and $H = 500 \mu\text{m}$ in the vertical direction. The boundary conditions are also shown in Figure 2b. Periodic condition was defined on the left and right side of the domain to simulate an infinitely long plate. The boundary surface with groove was defined as the no-slip boundary on which the air flow velocity was zero because of the viscosity. Symmetry conditions were set on the top side where the velocity was equal to the free stream velocity and the velocity and pressure no longer changed in the direction perpendicular to the surface.

2.2.2. Computational Setup

Ansys fluent was adopted in our numerical analysis. Air flow was used in the simulations and assumed that the property of air remained constant in simulation process. Reference density, temperature, and pressure of 1.225 kg/m^3 , $15 \text{ }^\circ\text{C}$, and $101,325 \text{ Pa}$ were

adopted in the simulation, respectively. What we examined in this study was the fluid details of the boundary layer near the groove surface. Based on this consideration, a large eddy simulation (LES) turbulence model was the best choice in our numerical analysis. Compared to the Reynolds-averaged turbulence model, LES has been applied to solve a variety of industry problems where higher calculation accuracy and more flow field information were needed. The transient solver was necessary for the simulations because of the time-varying nature of the flow field near the grooves. For pressure–velocity coupling, SIMPLE scheme was adopted to obtain a good convergence. The spatial discretization is important for computational accuracy stability. The second-order scheme and the bounded central difference were defined for the pressure and momentum. The least squared cell-based gradients were set for the gradient term. Time step for all simulations was set as 10^{-7} s. The residuals of the variables in the iterative process were used to judge the convergence of the calculation in the order of 10^{-5} .

2.3. Mesh Convergence Analysis

Structured mesh was adopted in the simulations, as shown in Figure 3, to improve grid quality. The minimum orthogonal quality of the mesh is about 0.6. The mesh convergence was performed on the smooth surface with 4 sets of meshes. The friction coefficient of the surface (C_f) was calculated in this analysis as

$$C_f = \frac{F_f}{\frac{1}{2}\rho U^2 A} \quad (1)$$

where F_f is the resistance of the surface, ρ and U are the density and freestream velocity of the air flow, respectively, and A is the reference area. The mesh convergence results are presented in Figure 4. The simulations using mesh 3 (M3) and mesh 4 (M4) have negligible differences to the resistance coefficient of the surface. As a result, we adopted the mesh type M3 in our simulations, as that had a high enough grid resolution.

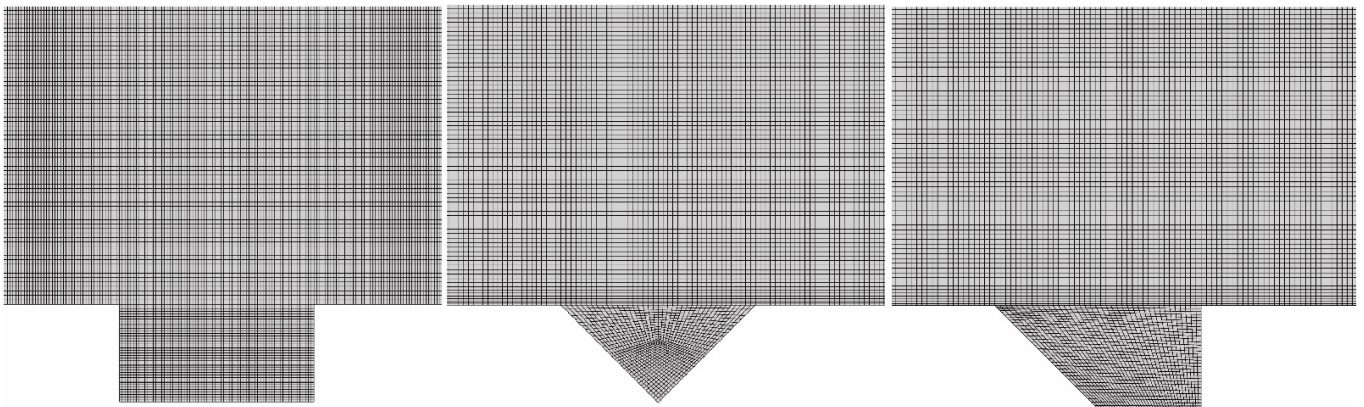


Figure 3. The structured mesh used in the numerical simulations for three types of grooves.

2.4. Experiment Methods

The wind tunnel experiment for the microstructures included two parts, one of which was a small-area microstructure constructed by machining on the surface of a cylinder, and the other was a large-area test constructed on a flat plate.

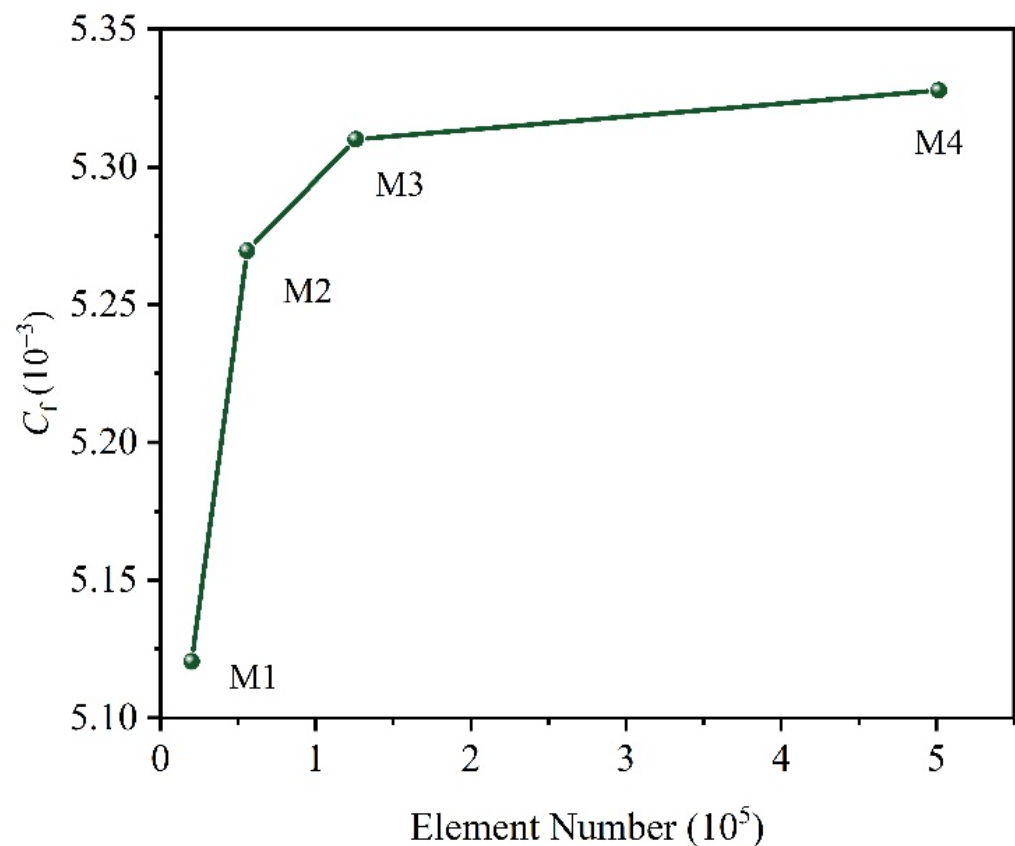


Figure 4. The results of mesh convergence analysis in the simulations.

2.4.1. Experiment Setup for Cylinder Model

The cylinder experiment was performed in a subsonic wind tunnel that had a rectangular test section of 3 m × 3 m (width × height) with the maximum velocity of 100 m/s. Figure 5a illustrates the sketch of the experiment. The diameter and length of the cylinder were 70 mm and 300 mm, respectively. The axis of the cylinder was parallel to the velocity direction. The groove direction was along the circumference of the cylinder, perpendicular to the direction of velocity. A bullet head was designed at the front end of the cylinder to obtain a better flow field. In addition, a tail block was set at the rear end of the cylinder to reduce the impact of pressure at the wake region. The gap between the tail block and the rear end was about 5 mm. A force balance fixed in the center of the cylinder was used to measure the drag of the test model. The balance was calibrated before experiments and the uncertainty was less than 0.07%. The whole test model was installed in the center of the wind tunnel by a support rod at the rear end. The support rod can change attach angle to ensure that the axis of the cylinder is parallel to the velocity direction during the experiment. The groove structures on the cylinder model were fabricated by machining method. The surface topography of the groove cylinder was measured by surface topography instrument, and the results are shown in Figure 5a. The groove shape on the cylinder surface was very close to the theoretical model and this was beneficial to verify the calculation results. Figure 5b,c present the pictures of wind tunnel experiments.

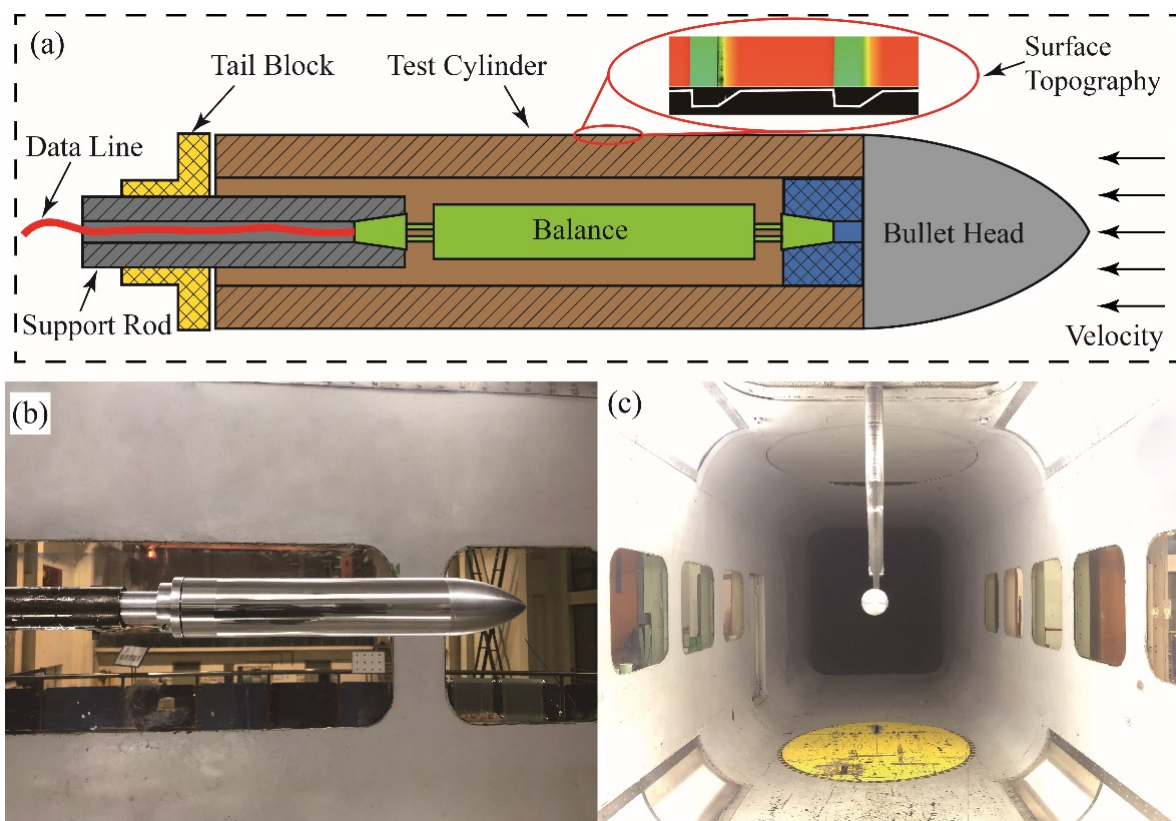


Figure 5. The experiment setup for the cylinder model: (a) the sketch of wind tunnel experiment for cylinder model; (b) and (c) are the pictures of the test model in the wind tunnel.

2.4.2. Experiment Setup for Plate Model

The drag reduction by grooves on the large surface area is an important characteristic for its applications. As a result, a large area plate with spanwise grooves was fabricated for experimentation. The plate experiment was performed in a subsonic wind tunnel that had a rectangular test section of $2\text{ m} \times 1.5\text{ m}$ (width \times height). Figure 6a illustrates the experiment setup. The lengths of the test plate were 1000 mm in streamwise direction and 1200 mm in spanwise direction. The test plate was mounted on the test base of the wind tunnel, and the front edge of the base was airfoiled to reduce the influence on the flow field on the plate.

It is difficult to measure the drag of the force balance in the wind tunnel due to the small drag force and large gravity of the plate. Therefore, an indirect method by measuring the pressure was adopted in this experiment. Two pressure-measuring positions were set at the front and rear ends of the plate, and the distance between them was 900 mm. The total pressure was measured by the measuring device on which the probes were installed at different heights to obtain the total pressure in the boundary layer. The static pressure was measured by the hole on the test plate near the measuring device. In order to prevent the impact of the pressure measuring device on the flow field, the pressure distribution in the front and rear of the plate was measured successively. Figure 6b,c are the pictures of pressure measuring at the front and rear of the plate in the wind tunnel. Figure 6d presents the picture of the pressure-measuring device used in the experiment.

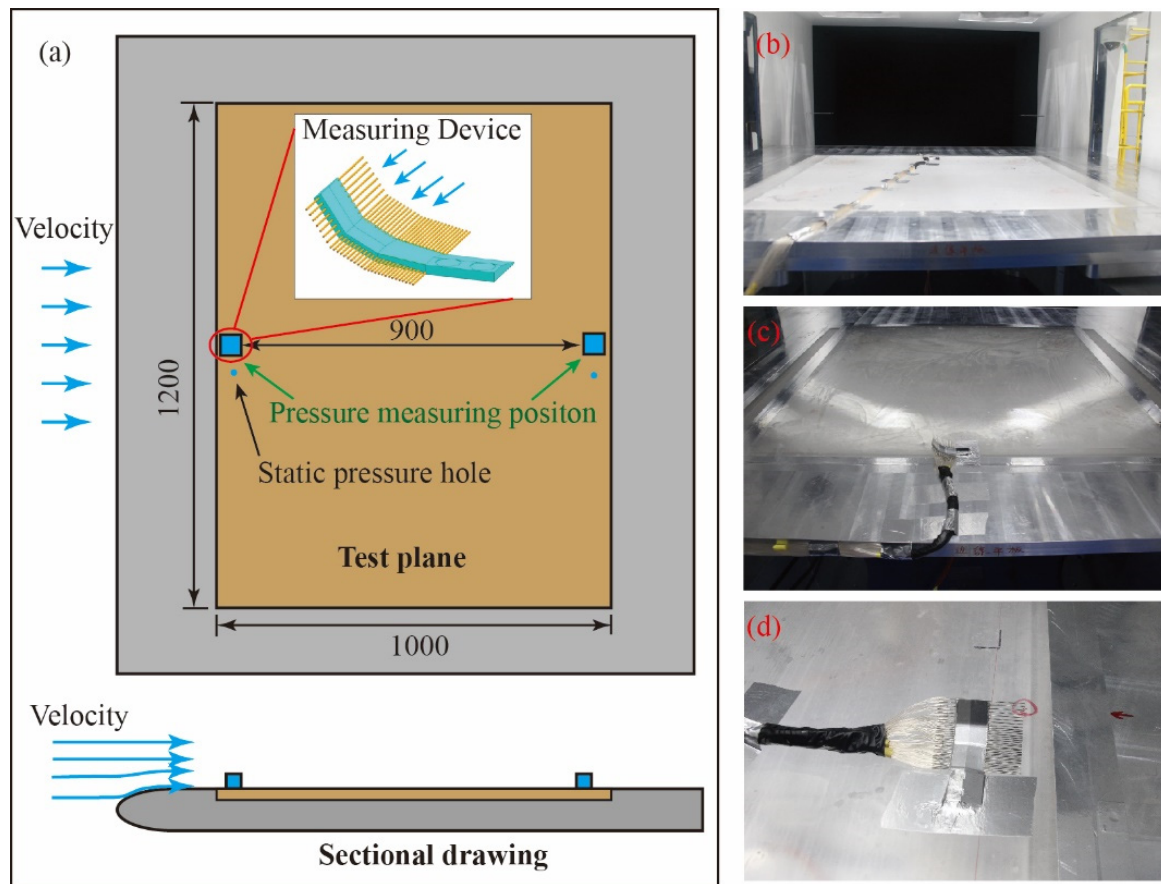


Figure 6. The experiment setup for the plate model: (a) the sketch of wind tunnel experiment for plate model; (b) pressure measuring at the front of the plate; (c) the pressure measuring at the rear of the plate; (d) the pressure-measuring device used in the experiments.

The drag of the plate was obtained by the velocity distribution in the boundary layer. Figure 7 present the control volume near the wall. According to the conservation of momentum, the equation can be written as

$$F_d = - \int_{I-I'} (\rho u) u dS - \int_{II-II'} (\rho u) u dS \quad (2)$$

where F_d is the drag of the wall, ρ and u represent the density and local velocity of the airflow, respectively. To ensure that the drag of the plate can be calculated if the velocity distribution has been measured, there is the following relationship between velocity and dynamic pressure:

$$Q = \frac{1}{2} \rho u^2 \quad (3)$$

where Q is the dynamic pressure ($Q = p_t - p_s$, where p_t is the total pressure and p_s is the static pressure). Therefore, the velocity distribution can be obtained only by measuring the pressure distribution in the boundary layer. In the actual wind tunnel test, the pressure values were time-averaged, so that the velocity distribution and the drag calculated by that were also time-averaged values.

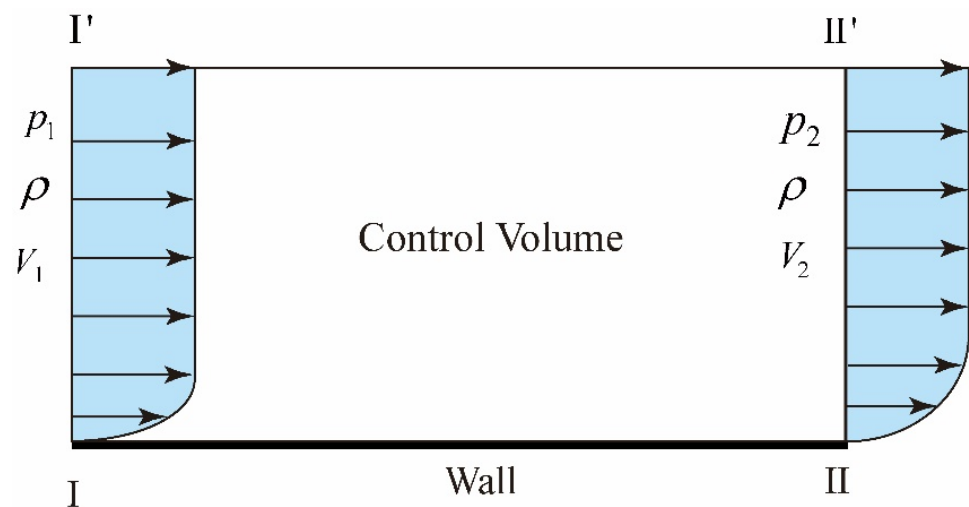


Figure 7. Schematic diagram of the control volume near the wall.

3. Results and Discussion

3.1. Fluid Field Profile

The fluid field profile is closely related to the drag of a surface. The CFD simulations on three types of grooves were conducted with a freestream velocity of 60 m/s. Figure 8 presents the time-averaged velocity field and streamline near the groove surface. It can be found that vortices are generated in the groove, and they have different forms because of the groove shape. The vortex was also reported by experiments with the rectangle groove [17]. Vortices are easier to form in rectangular groove than others and fill the entire groove, while vortices become smaller in the triangular groove and are located at the bottom. For the trapezoidal groove, vortices are easier to form than in the triangular groove. In the groove region, the original air–solid interface becomes air–air interface, which can reduce the wall shear stress obviously. This change is closely related to the vortices in the groove, which are discussed in detail later. For the macro-groove, secondary eddies were generated at the groove bottom [18], while for the groove in this simulation, there is only one vortex in the groove. This difference is due to groove size, which has obvious influence on the flow field.

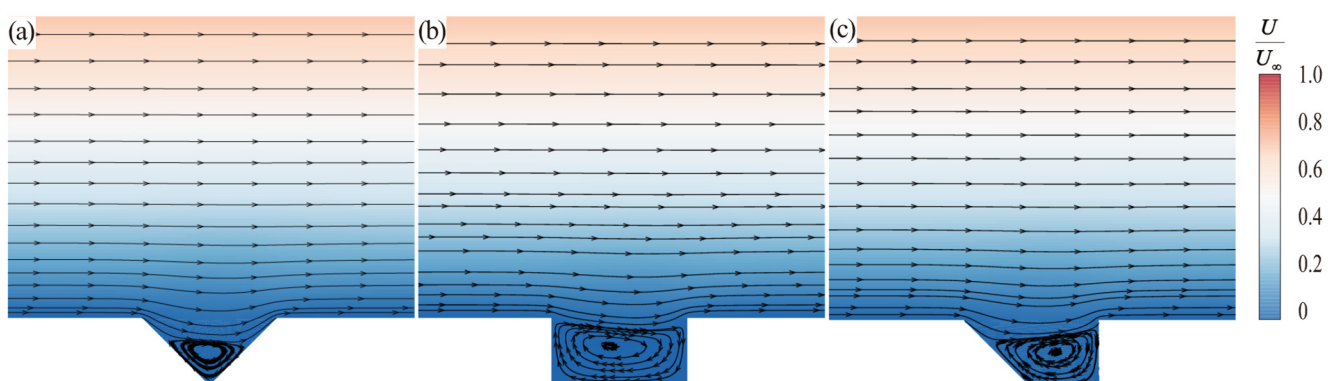


Figure 8. The streamline distribution near the groove where the map was colored by the dimensionless velocity U/U_∞ : (a–c) the three types of grooves of triangle, rectangle, and trapezoid, respectively.

Compared with the smooth surface, the pressure distribution on the groove surface has unique properties and is closely related to the resistance. The pressure coefficient discussed in this paper is defined as follows:

$$C_p = \frac{p}{\frac{1}{2}\rho U^2} \quad (4)$$

where p , ρ , and U are the static pressure, density, and freestream velocity, respectively. Figure 9 reveals the pressure coefficient distribution near the groove surface. The pressure difference between the two sides of the groove can be found from Figure 9. An additional drag is generated due to the pressure difference, and this does not happen on the smooth surface. There is a low pressure region on the left side and a high pressure region at the right pressure for the three types of grooves. By comparing the pressure distribution of the three types of grooves, the vertical side wall brings higher pressure on the right side and lower pressure on the left side, which leads to a higher pressure drag.

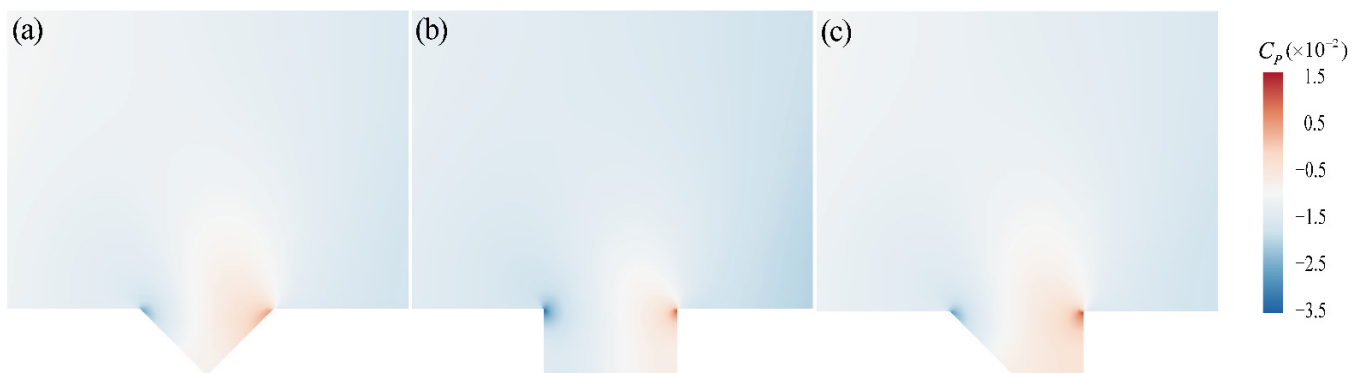


Figure 9. The pressure coefficient distribution near the groove: (a–c) the three types of grooves of triangle, rectangle, and trapezoid, respectively.

In order to analyze the distribution of shear stress and pressure on the groove surface more intuitively, the data of the groove surface in one period were extracted. Figure 10a presents the coordinates where the data were extracted. Figure 10b illustrates the distribution of dimensionless stress τ/τ_0 (where τ and τ_0 are the shear stress of groove and smooth surface, respectively). The wall shear stress at the groove region is significantly reduced, and is most obvious in the rectangular groove. Comparing the stress distribution of the three types of grooves, its main difference is concentrated on both sides of the grooves. The sloped side (meaning both sides of the triangular groove and the left side of the trapezoidal groove) is not beneficial in reducing the shear stress compared with the vertical side. As a result, the shear stress inside the rectangular groove with two vertical side walls is almost negligible. The shear stress distribution is closely related to the vortex shape in the groove (as shown in Figure 8). The shear stress is smaller while a larger vortex forms in the groove. Other numerical research also shows that the height between the vortex center and the bottom of the groove is related to the slip velocity at the groove region [21]. The contribution of the slip velocity to the drag reduction essentially reduces the wall shear stress. It should be noted that there are overshoots of wall shear stress at the two ends of the groove. This is because a slip velocity exists inside the groove, while both sides of the groove are non-slip walls. A sudden change in velocity in this region causes an increase in wall shear stress.

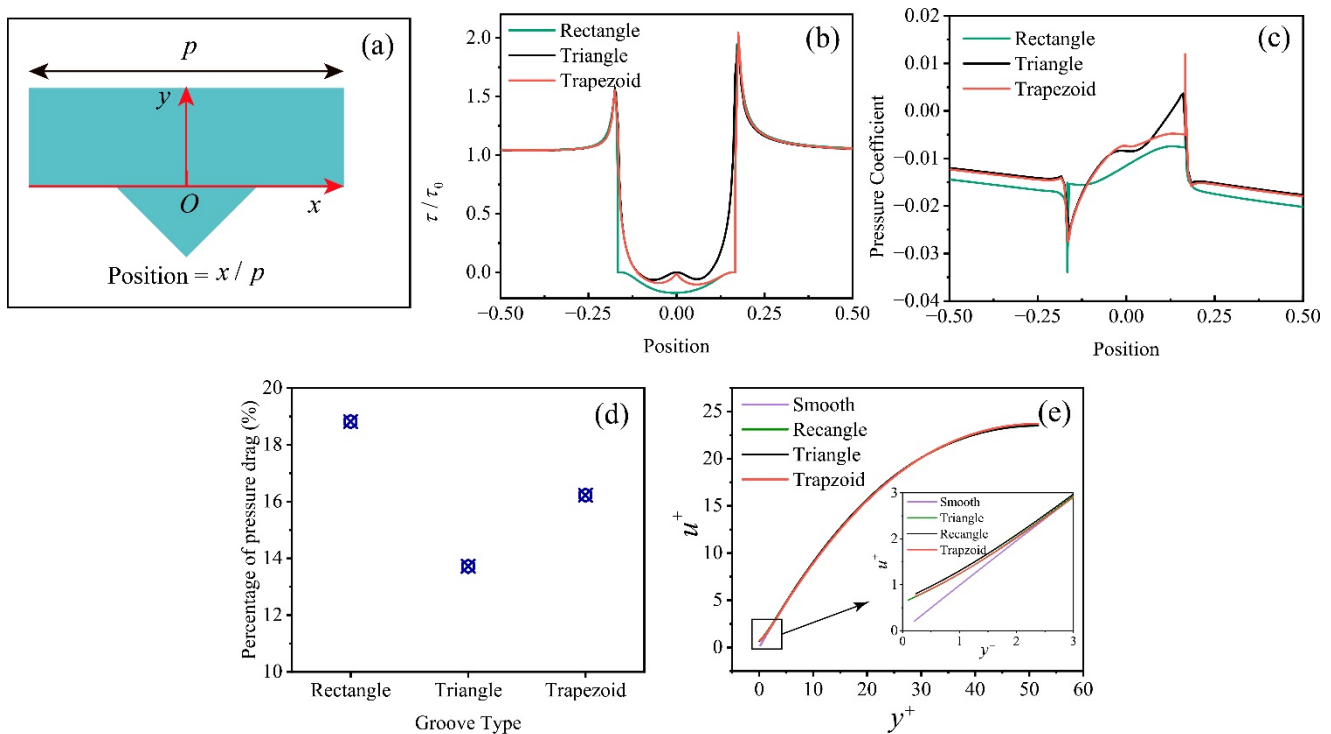


Figure 10. The fluid field profile near the surface: (a) the definition of the position using in this figure; (b,c) the dimensionless wall stress on three types of grooves; (d) the percentage of pressure drag to the total drag on the surface; (e) the velocity distribution near the groove and smooth surface.

The pressure profile on the groove wall is presented in Figure 10c. This profile is also related to the groove shape (Figure 8). There are low-pressure regions for all grooves on the left side, and the pressure on the left side of the rectangular groove is lower than the others. On the other hand, a higher pressure exists on the right side of the rectangle and trapezoidal grooves. The vertical side of the groove brings a greater pressure difference between the two sides, resulting in the greater additional pressure drag. Figure 10d illustrates the additional pressure drag percentage to total drag of the groove wall according to the simulation results. The percentage of the rectangular groove is as high as about 16%, while that of the triangular groove is only about 13%, and that of the trapezoidal groove is between the two. This result can also be verified from the pressure distribution (shown in Figure 8) and the pressure profile (Figure 10c). It follows that the rectangular grooves bring greater additional pressure drag while reducing frictional resistance, and triangular grooves act in an opposite fashion.

The velocity distribution along the y -axis is shown in Figure 10e. The dimensionless length and velocity are defined as $y^+ = yu_\tau/\nu$ and $u^+ = u/u_\tau$, where $u_\tau = \sqrt{\tau_0/\rho}$, and ρ , and ν are the density and kinematic viscosity of air flow, respectively. The range of the velocity distribution in the y direction is from $y^+ = 0$ to $y^+ = 50$. This is almost in the sublayer of the boundary where the viscosity has a great influence on the fluid field. It can be found from the velocity distribution that u^+ is proportional to y^+ at the near-wall region and the velocity on the surface of the three grooves is almost the same. The groove has little influence on the boundary layer. The velocity distribution is also shown at the region very near the surface in Figure 10e, where the velocity has a difference between the groove and smooth surfaces. The curve for the smooth surface has a larger slope in this area, which means that there is higher shear stress between the air flow and wall surface. However, for the groove of a larger size, such as millimeter-scale grooves, this has a great impact on the velocity distribution of the boundary layer [19]. The size parameters, such as depth and width of grooves, determine the impact on the fluid field.

3.2. Drag Results of Simulations and Experiment

The drag force of the groove surface consists of two parts, and the force equation can be calculated by:

$$F_d = \int_0^{\infty} (\boldsymbol{\tau} + p\mathbf{n}) \cdot \mathbf{e}_x ds \quad (5)$$

where $\boldsymbol{\tau}$ and $p\mathbf{n}$ are the vectors about shear stress and pressure, respectively; \mathbf{e}_x is the unit vector parallel to the velocity direction; and s denotes the unit area along the groove wall. Therefore, the drag reduction depends on the combination of shear stress and pressure. The drag reduction rate is defined as:

$$\eta = \frac{F_s - F_g}{F_s} \quad (6)$$

where F_s and F_g present the drag of smooth and grooved surfaces, respectively.

Figure 11a presents the drag reduction rate of simulation for three types of groove surfaces, as well as the experiment results of the cylinder and plate models at the velocity of 60 m/s. It can be found that the trapezoidal groove surface is more efficient in reducing the drag. Compared to the rectangular groove, the trapezoidal groove has smaller pressure drag because of the left sloped side. Vortices can be easily formed in the trapezoidal groove compared to the triangular groove, meaning that the wall shear stress becomes smaller. Based on the above factors, the drag reduction by the trapezoidal groove becomes the best one in simulations. Comparing the results of CFD and experiments, there is a big difference in the drag reduction rate. The reason for this is that a long enough surface was set in the numerical simulations, but the test cylinder and plate were of finite length, and the air flow did not develop enough due to the wind tunnel size in the experiment. In addition, the pressure drag of the cylinder model still exists during all experiments, so that the experiment result is smaller than that of the simulations. The drag reduction rate of the plate model is higher than CFD result because of the errors of CFD and experiments.

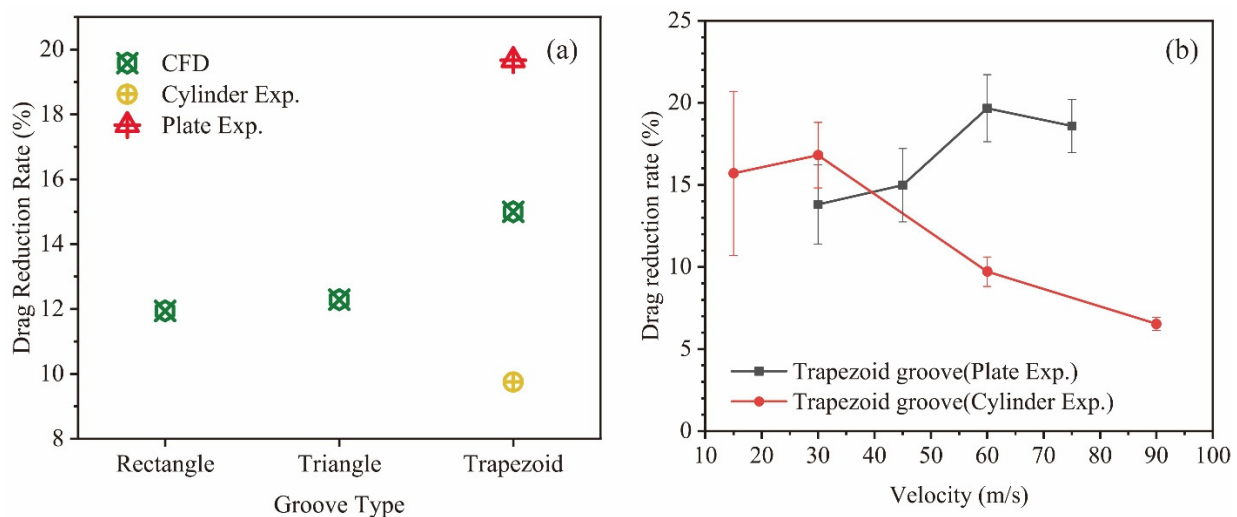


Figure 11. The drag reduction rate of CFD analysis and wind tunnel experiments: (a) the drag reduction rate of CFD analysis and experiment at the velocity of 60 m/s; (b) the drag reduction rate of experiments for cylinder and plate models.

The drag reduction rates of experiment results with respect to the velocity are shown in Figure 11b. A series of velocities from 15 m/s to 90 m/s were tested in the cylinder experiments. A significant drag reduction was obtained for all test velocities. The maximum drag reduction rate is about 16% at the velocity of 30 m/s, while it reduces to about 8.5% at the velocity of 60 m/s. It can also be found from Figure 11b that the drag reduction rate

decreases with the increase in velocity. This is probably due to the sharp increase in the pressure drag of the cylinder.

The test results of large-area plate model can better reflect the application potential of the microstructure surface. A series velocity of 30 m/s to 74 m/s was adopted in the plate experiment, and the drag reduction rate of that with the trapezoidal groove is shown in Figure 11b. Different from the direct measurement by force balance, the pressure measurement leads to an increase in uncertainty. Nevertheless, the surface with the trapezoidal groove still has a significant drag-reducing effect during the experiment. The drag reduction rate is about 19% at the velocity of 60 m/s. It is better than that of the numerical results (about 16%), which is also due to the infinite length assumption in the simulations. The drag reduction rate does not decrease with the increase in velocity according to the experiment results of the plate. Therefore, the drag-reducing property of the trapezoid groove surface can be effective in a wide range of velocities. Comparing the results of the cylinder and plate experiments, we find that the drag reduction rates are similar at low velocity, but differ greatly at high velocity. For a low velocity, the results of the cylinder are more referential than that of the plate, because the drag is measured by force balance directly and the pressure drag due to the shape is small, while at high velocity, the results of plate model are more meaningful.

4. Conclusions

The spanwise groove surface has a contribution to drag reduction due to the formation of vortices inside the groove. At the same time, the additional pressure difference between two sides of the groove leads to increased drag. The vertical groove wall, such as in a rectangle groove, reduces the wall shear stress more efficiently, but with the greater additional pressure drag. The sloped groove wall, such as in a triangle groove, is the opposite. The trapezoid groove achieves the highest drag reduction rate among the study cases according to the simulation results. The experiment results by using a cylinder model reveal that the trapezoid groove has a contribution to drag reduction at a series velocity of 15 m/s to 90 m/s, and the drag reduction rate is sensitive to the freestream velocity. The surface with a trapezoid groove also worked in drag reduction according to the experiment results of the large-area plate, which has referential significance for practical applications. The shape of the groove is an important parameter to deflect the drag. The dimensions, such as width and depth of groove, are also related to the drag-reduction effect, which requires further research.

Author Contributions: Conceptualization, J.W.; methodology, D.W.; formal analysis, Y.W. (Yanqing Wang); investigation, Y.W. (Yuju Wei); writing—original draft preparation, Y.W. (Yanqing Wang); writing—review and editing, D.W. All authors have read and agreed to the published version of the manuscript.

Funding: This research was funded by National Key R&D Program of China, (grant number 2020YFF0304600 and 2019YFF0302100) and the National Natural Science Foundation of China (grant number 52275200).

Data Availability Statement: Not applicable.

Conflicts of Interest: The authors declare no conflict of interest.

References

1. Bechert, D.W.; Bruse, M.; Hage, W.; Meyer, R. Fluid mechanics of biological surfaces and their technological application. *Naturwissenschaften* **2000**, *87*, 157–171. [[CrossRef](#)] [[PubMed](#)]
2. Bhushan, B. Biomimetics: Lessons from nature—An overview. *Philos. Trans. R. Soc. A Math. Phys. Eng. Sci.* **2009**, *367*, 1445–1486. [[CrossRef](#)] [[PubMed](#)]
3. Walsh, M.; Lindemann, A. Optimization and application of riblets for turbulent drag reduction. In Proceedings of the 22nd Aerospace Sciences Meeting, Reno, NV, USA, 9–12 January 1984. [[CrossRef](#)]
4. Walsh, M. Effect of Detailed Surface Geometry on Riblet Drag Reduction Performance. *J. Aircr.* **1990**, *27*, 572–573. [[CrossRef](#)]

5. Bechert, D.W.; Bruse, M.; Hage, W. Experiments with three-dimensional riblets as an idealized model of shark skin. *Exp. Fluids* **2000**, *28*, 403–412. [[CrossRef](#)]
6. Bechert, D.; Bruse, M.; Hage, W.; Meyer, R. Biological surfaces and their technological application—Laboratory and flight experiments on drag reduction and separation control. In Proceedings of the 28th Fluid Dynamics Conference, Village, CO, USA, 29 June–2 July 1997.
7. Koeltzsch, K.; Dinkelacker, A.; Grundmann, R. Flow over convergent and divergent wall riblets. *Exp. Fluids* **2002**, *33*, 346–350. [[CrossRef](#)]
8. Sundaram, S.; Viswanath, P.R.; Rudrakumar, S. Viscous drag reduction using riblets on NACA 0012 airfoil to moderate incidence. *AIAA J.* **1996**, *34*, 676–682. [[CrossRef](#)]
9. Subaschandar, N.; Kumar, R.; Sundaram, S. Drag Reduction Due to Riblets on a GAW(2) Airfoil. *J. Aircr.* **1999**, *36*, 890–892. [[CrossRef](#)]
10. Zhang, D.-y.; Luo, Y.-h.; Li, X.; Chen, H.-w. Numerical Simulation and Experimental Study of Drag-Reducing Surface of a Real Shark Skin. *J. Hydrodyn.* **2011**, *23*, 204–211. [[CrossRef](#)]
11. Li, C.; Tang, S.; Li, Y.; Geng, Z. Numerical and experimental investigations on drag-reducing effects of riblets. *Eng. Appl. Comput. Fluid Mech.* **2021**, *15*, 1726–1745. [[CrossRef](#)]
12. Qiu, H.; Chauhan, K.; Lei, C. A numerical study of drag reduction performance of simplified shell surface microstructures. *Ocean. Eng.* **2020**, *217*, 107916. [[CrossRef](#)]
13. Ko, N.W.M.; Leung, Y.C.; Chen, J.J.J. Flow past V-groove circular cylinders. *AIAA J.* **1987**, *25*, 806–811. [[CrossRef](#)]
14. Cheng, W.; Pullin, D.I.; Samtaney, R. Large-eddy simulation of flow over a grooved cylinder up to transcritical Reynolds numbers. *J. Fluid Mech.* **2017**, *835*, 327–362. [[CrossRef](#)]
15. Kimura, T.; Tsutahara, M. Fluid dynamic effects of grooves on circular cylinder surface. *AIAA J.* **1991**, *29*, 2062–2068. [[CrossRef](#)]
16. Ranjan, P.; Ranjan, A.R.; Singh, A.P. Computational analysis of frictional drag over transverse grooved flat plates. *Int. J. Eng. Sci. Technol.* **2011**, *3*, 110–116. [[CrossRef](#)]
17. Sutardi, S.; Widodo, W.A. Analysis of Turbulence Characteristics in the Laminar Sub-Layer Region of a Perturbed Turbulent Boundary Layer. *Appl. Mech. Mater.* **2016**, *836*, 115–120. [[CrossRef](#)]
18. Sutardi; Ching, C.Y. The response of a turbulent boundary layer to different shaped transverse grooves. *Exp. Fluids* **2003**, *35*, 325–337. [[CrossRef](#)]
19. Ahmadi-Baloutaki, M.; Carriveau, R.; Ting, D.S.K. Effect of free-stream turbulence on flow characteristics over a transversely-grooved surface. *Exp. Therm. Fluid Sci.* **2013**, *51*, 56–70. [[CrossRef](#)]
20. Tirandazi, P.; Hidrovo, C.H. Study of drag reduction using periodic spanwise grooves on incompressible viscous laminar flows. *Phys. Rev. Fluids* **2020**, *5*, 064102. [[CrossRef](#)]
21. Li, Z.; He, L.; Zheng, Y. Quasi-Analytical Solution of Optimum and Maximum Depth of Transverse V-Groove for Drag Reduction at Different Reynolds Numbers. *Symmetry* **2022**, *14*, 342. [[CrossRef](#)]
22. Wu, Z.; Yang, Y.; Liu, M.; Li, S. Analysis of the influence of transverse groove structure on the flow of a flat-plate surface based on *Liutex* parameters. *Eng. Appl. Comput. Fluid Mech.* **2021**, *15*, 1282–1297. [[CrossRef](#)]

Disclaimer/Publisher’s Note: The statements, opinions and data contained in all publications are solely those of the individual author(s) and contributor(s) and not of MDPI and/or the editor(s). MDPI and/or the editor(s) disclaim responsibility for any injury to people or property resulting from any ideas, methods, instructions or products referred to in the content.